



## Impacts of anthropogenic aerosols on a snowfall event – A case study in the Guanzhong Basin and its surrounding areas, China

Yuning Yang<sup>1</sup>, Naifang Bei<sup>1\*</sup>, Ruonan Wang<sup>2</sup>, Qing Ji<sup>1,3</sup>, Haiyue Hong<sup>1</sup>, Zhe Li<sup>1</sup>, Xuexi Tie<sup>2</sup>,  
5 and Guohui Li<sup>2\*</sup>

<sup>1</sup>School of Human Settlements and Civil Engineering, Xi'an Jiaotong University, Xi'an, 710049, China

<sup>2</sup>State Key Laboratory of Loess Science, Institute of Earth Environment, Chinese Academy of Sciences, Xi'an 710061, China

10 <sup>3</sup>Shaanxi Meteorological Observatory, Xi'an, 710014, China

*Correspondence to:* Naifang Bei (bei.naifang@mail.xjtu.edu.cn) and Guohui Li (ligh@ieecas.cn)

**Abstract.** Impacts of anthropogenic aerosols on clouds and snowfall during winter precipitation events remain highly uncertain, particularly under heavy pollution. A winter snowfall event over the Guanzhong Basin (GZB) and its surrounding regions (GZBs), China, has been simulated using a cloud-resolving, fully coupled WRF-Chem  
15 model to quantify the respective roles of aerosol–radiation interactions (ARIs) and aerosol–cloud interactions (ACIs). The simulated temporal variation and spatial distribution of air pollutants and precipitation generally agree with the observations in the GZB+GZBs. Sensitivity experiments are performed to evaluate effects of ARIs and ACIs by changing the anthropogenic emissions. The precipitation response to ARIs and ACIs exhibits regional contrast in GZB and GZBs due to different aerosol concentrations. In the GZB, exclusion of ARIs leads  
20 to a slight increase in precipitation with increasing emissions, mainly associated with enhanced ice-phase precipitation induced by ACIs. ARIs increase the precipitation in the GZB when emissions increase reaches a threshold, caused by ARI-induced enhancement of relative humidity (RH) which increases ice water path and favors survival of falling ice particles. In contrast, precipitation in the GZBs decreases with increasing emissions, reflecting suppression of liquid-phase precipitation by ACIs and reductions in RH caused by ARIs. In addition,  
25 changes in anthropogenic emissions exert limited influence on the spatial distribution of precipitation across the combined GZB–GZBs region. These findings provide process-level insight into how ARIs and ACIs regulate snowfall under polluted conditions, with implications for improving aerosol–precipitation coupling in regional climate and weather models.



## 30 1 Introduction

Anthropogenic aerosols can directly and indirectly modulate the dynamics, thermodynamics, and microphysics of the cloud-precipitation process by absorbing or scattering the solar radiation and serving as cloud condensation nuclei (CCN) or ice nuclei (*IN*) (e.g., Boucher et al., 2013; IPCC 2013; Huang and Ding, 2021; Zhao et al., 2024), constituting one of major uncertainties in climate prediction and weather forecasting (e.g., Quaas, 2015; Myhre et al., 2013; Makar et al., 2015; IPCC 2021). Aerosol effects on the solar radiation are referred as to aerosol-radiation interactions (ARIs), which traditionally include the direct and semi-direct effects (e.g., Charlson et al., 1992; Sun and Zhao, 2021; Ackerman et al., 2000). Aerosol effects on CCN and IN and further cloud-precipitation are referred as to aerosol-cloud interactions (ACIs), which is also called aerosol indirect effect (e.g., Mitchell, 1971; Braham, 1974; Twomey, 1977; Albrecht, 1989).

40 Past studies have proposed many mechanisms about aerosol effects on precipitation, such as the positive precipitation-aerosol relationships attributed to invigoration effect (e.g., Khain et al., 2005; Pinsky et al., 2013; Rosenfeld et al., 2008), the negative aerosol effect on precipitation due to cloud water competition (e.g., Albrecht, 1989; Rosenfeld, 1999), wet scavenging (e.g., Grandey et al., 2014), and decreased solar radiation (e.g., Ackerman et al., 2000; Koren et al., 2004). The two mechanisms proposed for the invigoration effect include (1) mixed- or  
45 cold-phase invigoration, whereby aerosol induced higher CCN suppress warm-rain formation, resulting in greater lofting of cloud condensate mass and increased fusion heating as the droplets freeze (e.g. Rosenfeld et al., 2008), and (2) warm-phase invigoration, whereby aerosol induced higher CCN increase condensation heating (e.g. Kogan and Martin, 1994; Pinsky et al., 2013). It is worth noting that the invigoration effect is still debatable due to insufficient observational evidence or flawed methodology (e.g., Öktem et al., 2023; Romps et al., 2023; Varble et al., 2023).

50 However, the net effect of aerosols on clouds and precipitation remains controversial and depends on many factors, including meteorological conditions, specific aerosol loadings, cloud/precipitation types, cloud/precipitation development stages, aerosol composition and size distribution, relative location of aerosol and cloud vertical locations, and orography conditions (e.g. Khain et al., 2008; Tao et al., 2007; Guo et al., 2018; Guo et al., 2014; Zhang et al., 2002; Ackerman et al., 2000; Yang and Li, 2014). First, the aerosol effect on precipitation depends on different types of precipitation. For example, aerosols can enhance convective precipitation but inhibit stratiform precipitation, which lead to intensified flooding in southern China in summer and aggravated drought in East Asia' s middle and low latitudes area especially during winter and spring time (e.g., Menon et al., 2002; Zhang et al., 2017; Huo et al., 2021; Xie et al., 2022; Ryu et al., 2022; Sun et al., 2022). Second, aerosol effect on  
60 precipitation varies with precipitation grade. Studies show that increasing aerosol concentrations can enhance heavy rain but reduce moderate and light rain, which may also reduce the frequency of the moderate and light rain (e.g., Wang et al., 2011; Shao et al., 2022). Third, the specific impact of aerosols on precipitation varies across different phases of precipitation process due to the competition between ARIs and ACIs (e.g., Lee et al., 2016). Furthermore, the influence of aerosols on precipitation also relies on the position of aerosols. As an example, low-  
65 level anthropogenic aerosols inhibit the precipitation process while high-level aerosols enhance it (e.g., Bai et al., 2020; Sun et al., 2022). Most recently, Yun et al. (2024) have found that aerosol effects on MCS-averaged precipitation is mostly similar between the polluted and clean conditions due to compensations among the subregions with divergent spatiotemporally discretized changes. Wang et al. (2024) have emphasized the aerosol



IN effect on cloud microphysics, convection intensity, and regional rainfall distribution. Peng et al. (2025) have  
70 pointed out that aerosols exert stronger impacts on convective than stratiform precipitation as mentioned in Sun  
and Zhao (2021) based on data analysis. Moraglia and Crippa (2026) have also indicated that differences induced  
by land-use perturbation and aerosols is smaller in stratiform rain than that in convective rain because the absence  
of strong vertical mixing prevents the activation of more aerosols.

Given the complexity of precipitation phase states, there has been relatively limited exploration into how  
75 aerosols influence wintertime precipitation processes, especially snowfall event (e.g., Saleeby et al., 2010;  
Thompson and Eidhammer, 2014; Guo et al., 2021; Cao et al., 2021; Zhang et al., 2022; Xiao et al., 2022; Pravia-  
Sarabia et al., 2023). Saleeby et al. (2010) have showed that an increase in aerosol concentrations results in a  
spillover of snowfall from the windward slope to the leeward slope, but the impact is largely controlled by the  
synoptic-scale flow and available moisture. Guo et al. (2021) have indicated that increased aerosol number  
80 concentrations have less impact on snowfall at the initial period due to the lower supersaturation produced by the  
urban heat and dry island but increase snowfall in the later period due to higher supersaturation caused by the  
feedback of the cloud microphysics. Based on sensitivity simulations of a winter extreme mixed-phase storm,  
Pravia-Sarabia et al. (2023) have indicated that the total precipitation remains basically unchanged, with  
maximum changes of 5% while the production of snow is largely altered.

85 Guanzhong Basin (GZB) is surrounded by the Loess Plateau to the northwest and Qinling Mountain to the  
south (Figure 1). Due to fast-growing industries and city expansions, the aerosol loadings inside the basin have  
been elevated during the past 3 decades, particularly during wintertime (e.g., Bei et al., 2016a; 2016b; 2017b).  
Aerosol effects on precipitation over the mountain area and inside the GZB have been investigated based on  
observational data at Mt. Hua's summit and its surrounding area (e.g., Rosenfeld et al., 2007; Yang et al., 2013a;  
90 2013b). Rosenfeld et al. (2007) have found that the precipitation at Mt. Hua in the south of GZB could be  
decreased by 30 to 50% during hazy conditions. Yang et al. (2013a; 2013b) have further pointed out that the  
decreasing trend of precipitation is correlated well with deterioration of the air pollution at Mt. Hua and inside the  
GZB, supporting the hypothesis that both aerosol microphysical and radiative effects could reduce precipitation.  
Most recently, based on sensitivity simulations of a summertime short-term heavy rainfall event under different  
95 aerosol scenarios, Bei et al. (2025) have shown that the synergetic effect of ARIs and ACIs consistently decreases  
the precipitation both in the whole simulation domain and GZB with increasing aerosols, but ARIs play a more  
important role in the decreasing trend of the precipitation with deterioration of PM pollution as mentioned in Zhou  
et al. (2024).

The present study aims to investigate the synergetic effects of ARIs and ACIs on a snowfall event occurred  
100 in the GZB and GZB surrounding areas (GZBs) using a fully coupled cloud-resolving WRF-Chem model. The  
model and experiment design are described in Section 2. The main results and discussion are presented in Section  
3. The conclusions are given in Section 4.

## 2 Model, data, and experiments design

### 2.1 WRF-Chem model configuration and experimental design

105 A specific version of WRF-Chem model, incorporating original contributions by Grell et al. (2005) and  
modifications by Li et al. (2010, 2011a, b, 2012), is employed to investigate the impact of anthropogenic aerosols



on a snowfall event occurred in the GZB and GZBs from 26 to 28 January 2022. We use Goddard shortwave module developed by Chou and Suarez (1999) and Chou et al. (2001) to consider the ARIs. The ACIs are evaluated using a two-moment bulk microphysics scheme developed by Morrison et al. (2009). Detailed model description of the WRF-Chem model, including the aerosol radiative module to calculate aerosol optical properties and the aerosol microphysical module to consider activation of aerosols to CCN and IN, can be found in Supplement Information (SI, SI-1, SI-2, and SI-3).

The model is configured with one domain using the grid spacing of 6 km for a total of  $500 \times 500$  grid points in the east-west and south-north directions, respectively, and the domain is centered at Xi'an ( $34.25^\circ\text{N}$ ,  $109^\circ\text{E}$ ) (Figure 1a). Figure 1b shows the study area, which is divided into two parts: GZB and its surrounding areas (GZBs). We use GZB+GZBs to represent the study area. The vertical direction is divided into 35 layers extending from the surface to 50 hPa, with a stretched vertical grid spacing ranging from 30 m near the surface, to 500 m above 2.5 km to achieve a finer vertical resolution within the planetary boundary layer. The meteorological initial and boundary conditions are derived from 6-hourly  $1^\circ \times 1^\circ$  NCEP-FNL (National Centers for Environmental Prediction final operational global gridded analysis). The chemical initial and boundary conditions are interpolated from the 6-h output of a global chemical transport model for ozone and related chemical tracers (MOZART) (Horowitz et al., 2003).

The model is integrated for a 126-h period from 1200 UTC 23 to 1800 UTC 28 January 2022 and the simulations from 1600 UTC 25 to 1600 UTC 28 are analyzed. In order to examine the effect of aerosols with different concentrations on the 3-day snowfall event, we first change the atmospheric aerosol concentrations via scaling the anthropogenic emissions of all species in the model. A set of 19 anthropogenic emission scale factor (AESF) is used in sensitivity simulations, ranging from  $2^{-3}$  to  $2^3$  with an exponential increasing step of 1/3. Then we design two groups of experiments to verify the contribution of ARIs, ACIs and the both to precipitation. In the first group sensitivity simulations, both ARIs and ACIs are considered with the AESF ranging from  $2^{-3}$  to  $2^3$  (hereafter referred as to F\_BASE). The second group of sensitivity simulations is the same as the F\_BASE, but the ARI effect is not considered (hereafter referred as to F\_ARI0). The model setup is the same for all experiments, except for the anthropogenic emission amplitude and the option of ARIs (on or off). In the F\_BASE, the member with the AESF of 1.0 is referred to as the benchmark simulation (CTRL), which is used to validate the model performance.

## 2.2 Model validation and statistical metrics

Hourly precipitation observational data for the GZB and GZBs stations are provided by the China Meteorological Administration (CMD) service center (<http://data.cma.cn/>), and hourly observations of  $\text{PM}_{2.5}$ ,  $\text{O}_3$ ,  $\text{NO}_2$ , and  $\text{SO}_2$  are released by the Ministry of Ecology and Environment of China. Three statistical metrics, including the normalized mean bias (NMB), root mean square error (RMSE), and the index of agreement (IOA) are used to evaluate the model performance. The population mean ( $p$ -mean hereinafter) of a given variable across all qualified grid points is applied to verify the general impact of aerosols on cloud properties. Detailed description about NMB, RMSE, IOA and  $p$ -mean can be found in SI-4.

## 3 Results and discussion



### 3.1 Snowfall event overview

145 A heavy snowfall event occurred from 26 to 28 January 2022 is investigated in GZB+GZBs, with the total  
precipitation of 6.4 mm, and the maximum daily precipitation of 2.3 mm is on January 28. Meanwhile, despite  
the occurrence of the snowfall event, the observed PM<sub>2.5</sub> concentrations ([PM<sub>2.5</sub>]) are still high during the three  
days, with the average of 108.5 and 74.1  $\mu\text{g m}^{-3}$  in GZB and GZBs, respectively. The snowfall event is basically  
the result of the interaction between the northerly cold air and southerly and easterly warm air in low-level  
150 atmosphere, as a cold front system proceeds from the North China (January 25) to the south-east (January 26-27)  
and then south-west direction (January 28) mainly along the coast (Figure S1). GZB+GZBs is located to the  
southwest (January 25), the west (January 26) and the northwest (January 27-28) side of the cold front, which is  
not the main area of the precipitation that occurred near the cold front. During January 26 to 28, there is clear  
evidence of weak cold air incursion in the GZB+GZBs at 925 hPa (Figures S2a-c). At 850 and 700 hPa (Figures  
155 S2d-i), the weak cyclonic wind shear and positive vorticity are maintained in the GZB during the event. At 500  
hPa (Figures S2j-l), GZB+GZBs is situated in the front of a very shallow trough, which is favorable for the  
development of low-level convergence, and eventually leads to the snowfall event in this area. The low-level  
water vapor is brought to the snowfall area mainly by the southwesterly and easterly airflow from Bay of Bengal  
and the South China Sea.

### 160 3.2 Model Evaluations

Figure 2 shows the pattern comparison of simulated PM<sub>2.5</sub>, O<sub>3</sub>, NO<sub>2</sub>, and SO<sub>2</sub> concentrations averaged during  
the study period with observations at monitoring sites in GZB and GZBs. The model generally reproduces the  
spatial distribution of air pollutants when comparing to observations. The simulated [PM<sub>2.5</sub>] are generally more  
than 75  $\mu\text{g m}^{-3}$  in the GZB, but the SO<sub>2</sub> level is not high in GZB and GZBs, less than 20  $\mu\text{g m}^{-3}$ . Figure 3 presents  
165 the simulated and observed time series of average hourly mass concentrations of PM<sub>2.5</sub>, O<sub>3</sub>, NO<sub>2</sub>, and SO<sub>2</sub>  
at monitoring sites in the GZB+GZBs from 26 to 28 January 2022. The model reasonably simulates the temporal  
variation of PM<sub>2.5</sub>, O<sub>3</sub>, and NO<sub>2</sub> concentrations, with the IOA exceeding 0.60. However, the model does not show  
good performance in simulating the SO<sub>2</sub> temporal variation, with an IOA of 0.25. In general, the model slightly  
underestimates the air pollutants concentrations against observations, with the NMB ranging from -8.4% to -2.3%.

170 Figure 4 provides the temporal variation of precipitation rates averaged at meteorological sites in  
GZB+GZBs from 26 to 28 January. The model generally yields the temporal variation of the hourly rainrate  
against observations, with the NMB and IOA of -3.3% and 0.85, respectively. The observed five rainrate peaks  
are successfully reproduced, but the underestimation of the first and fifth rainrate peak is considerable. The pattern  
comparison of the 3-day accumulative precipitation over the GZB+GZBs is shown in Figure 5. The model  
175 generally replicates the precipitation distribution compared to the observations (Figure 5a), with the NMB and  
IOA of -3.7% and 0.85, respectively. However, there exist underestimation of precipitation in the west part of the  
GZB.

### 3.3 Effects of ARIs on meteorological fields in GZB+GZBs

Figure 6a and 6b provide the variation of near-surface [PM<sub>2.5</sub>] and black carbon concentrations ([BC])  
180 averaged in the GZB+GZBs during the study period with increasing AESF. Near-surface [PM<sub>2.5</sub>] and [BC]  
generally increase with increasing AESF linearly. The ARI effect tends to hinder development of planetary



boundary layer (PBL) and decrease the PBL height (PBLH), increasing the near-surface concentration of air pollutants. Sensitivity results show that when the AESF increases from 0.125 to 8.0, the PBLH is decreased by about 34% in GZB+GZBs. The quasi-linear relationship between  $[PM_{2.5}]$  and AESF reflects that the variation of  
185  $[PM_{2.5}]$  with the AESF is mainly influenced by the emission of primary aerosols and the precipitation change caused by ARIs and ACIs. In addition, it is worth noting the decreased PBLH is also favorable for the formation of secondary aerosols, including sulfate, nitrate, ammonium, and secondary organic aerosol (SOA). However, secondary aerosols are generally water-soluble, and easily removed by wet deposition or activated to form cloud droplets. The aerosol optical depth (AOD) and absorbing AOD show the similar increasing relationship with the  
190 AESF in GZB+GZBs as that of  $[PM_{2.5}]$  and [BC]. The average AOD and AAOD in GZB+GZBs are 0.58 and 0.071 in the CNTL case, respectively, and the single scattering albedo is about 0.88, indicating a strong absorbing atmosphere over GZB+GZBs.

ARIs include direct scattering and/or absorbing of incident solar radiation by atmospheric aerosols and the induced adjustments of the surface energy budget, thermodynamic profile and cloudiness (IPCC, 2013). Therefore,  
195 aerosols in the atmosphere reduce the solar radiation down to the Earth surface and further sensible heat flux to the atmosphere, lowering the temperature of low-level atmosphere. Furthermore, light-absorbing aerosols also heat the atmosphere. Figure 7a shows the effect of ARIs on the temperature profile averaged in GZB+GZBs during the study period by differentiating the  $F_{BASE}$  and  $F_{ARI0}$  under various aerosol conditions. ARIs decrease the air temperature of the low-level atmosphere, and the air temperature decrease is mainly concentrated  
200 below 1.8 km and becomes increasingly significant with decreasing height or increasing AESF (Figure 7a). Previous studies have reported that absorbing aerosols cause a warming effect above the PBL (Ding et al., 2016; Gao et al., 2016; Wilcox et al., 2016; Wu et al., 2025). However, in the study, the average PBLH over GZB+GZBs decreases from about 450 m to 300 m with the AESF increasing from 0.125 to 8.0 in the  $F_{BASE}$ , but the warming layer is generally above 1.8 km and can extend to 7~8 km with the AESF exceeding 0.5. During the study period,  
205 the profile of vertical velocity shows occurrence of downdraft within the PBL and updraft above the PBL (Figure S3a). The cooling effect of ARIs within the near-surface atmosphere induces a downward motion and meanwhile an upward motion is generated above the PBL, which is resulted from the warming effect caused by absorbing aerosols and enhanced convergence by the ARI-induced downward motion (Figure 7b). Therefore, the upward motion above the PBL is enhanced by ARIs and more warm and moist air in the lower layer is being transported  
210 upward. The ARI-enhanced downward motion within the near-surface atmosphere is subject to transporting more air in the upper layer downward, causing a dry and cold effect, as shown in Figure 7c.

### 3.4 Response of cloud microphysic properties to aerosols

The impact of aerosols on cloud and precipitation is mediated by the combined effects of ACIs and ARIs (Twomey, 1977; Albrecht, 1989). Figure 8a presents the dependence of the column number density (CND) of  
215 cloud droplets and ice crystals over GZB+GZBs during the study period on the AESF. Increasing anthropogenic emissions escalate aerosol concentrations in the atmosphere, providing more CCN and IN to activate to form cloud droplets and ice crystals. Without ARIs, the CND of cloud droplets increases monotonically with increasing AESF, and the impact of increasing AESF on the CND of cloud droplets is not very significant, i.e., when the AESF increases from 0.125 to 8.0 or anthropogenic emissions increase by 64 times, the CND increases by 9.2  
220 times. However, the CND of ice crystals is not sensitive to increasing anthropogenic emissions. The different



response of cloud droplets and ice crystals to change of anthropogenic emissions is mainly caused by their formation at different height. The cloud water is mainly formed in the atmosphere below 3km, which is more susceptible to the influence of anthropogenic emissions (Figure S3b). However, the formation of ice crystal is concentrated in the atmosphere between 4 and 7 km, which is less affected by anthropogenic emissions due to  
225 downward motion within the PBL and continuous wet deposition processes (Figure S3c).

Furthermore, the CND of ice crystals generally decreases with increasing AESF, which is not consistent with the hypothesis that increasing anthropogenic emissions provide more IN to promote the formation of ice crystals. Since the formation of ice crystals is sensitive to relative humidity (RH), the possible reason for the decreasing trend with the AESF is that ACIs alter the RH in the atmosphere due to increasing anthropogenic emissions. In  
230 the F\_ARI0, the simulation using an AESF of  $2^{-3}$  is referred to as the reference simulation (REF0). For discussion convenience, we define the RH relative to water surface as RHW and the RH relative to ice surface as RHI. Figure S4 presents the impact of ACIs on the RHW and RHI profile averaged in GZB+GZBs during the study period by differentiating all members in F\_ARI0 with REF0. ACIs generally decrease RHW and RHI in the atmosphere and the decrease in RHW and RHI becomes significant with increasing AESF. Therefore, decreasing RHI with  
235 increasing AESF causes the decreasing trend of the CND with the AESF. In addition, decreasing RHW also explain the slow increase of the CND of cloud droplets with increasing AESF (Figure 8a).

When ARIs are considered, the CND of cloud droplets shows an increasing trend with the AESF when the AESF is less than 2.5, and when the AESF is more than 2.5, the CND decreases with the AESF, which is inconsistent with the Twomey effect (Twomey, 1977). In addition, ARIs decrease the CND at the same AESF,  
240 and with the AESF exceeding 2.5, the CND decrease is more than 20% (Figure 8b). As shown in Figure 7, ARIs adjust the profile of air temperature and specific humidity, further modifying the profile of RH. Figure S5a shows impacts of ARIs on the RHW profile averaged in GZB+GZBs during the study period by differentiating the F\_BASE and F\_ARI0. ARIs decreases RHW in the atmosphere below 3km where the cloud droplets are formed (Figure S3b), and the RHW decrease becomes increasingly significant with increasing AESF. Decreased RHW is  
245 not favorable for the formation of cloud droplets, so with the same AESF, ARIs decrease the CND of cloud droplets, as shown in Figure 8b. ARIs progressively decrease RHW with increasing AESF, continuously decreasing activity ability of CCN. Therefore, although increasing anthropogenic emissions provide a large amount of CCN, most of CCN can not be activated due to decreased RH. There exist a threshold AESF (2.5) beyond which the CND commences to decrease (Figure 8a). For ice crystals, impacts of ARIs on the CND is  
250 generally not significant with the AESF less than 1.0 (Figure 8c), and the CND variation due to ARIs is in the range between -0.5% and 0.5% (Figure 8d). When the AESF is more than 1.0, ARIs consistently increase the CND of ice crystals with increasing AESF. The main reason is that with the AESF exceeding 1.0, ARIs increase RHI in the atmosphere between 4 and 7km, enhancing the formation of ice crystals (Figure S5b).

In the F\_ARI0 without ARIs, cloud water path (CWP) decreases with increasing AESF. Many studies have  
255 proposed that increased CCN reduce cloud particle sizes to decrease the efficiency of collision and collection and further hinder auto conversion of cloud water to rainwater, causing more cloud water to exist in the atmosphere (e.g., Li et al., 2018; 2019). The decreasing trend of CWP with the AESF is caused by the decrease in RHW due to ACIs on the one hand (Figure 9a), as shown in Figure S5a. On the other hand, the presence of a large amount of small cloud droplets in the atmosphere is also beneficial for the collection of cloud water by ice-phase particles.  
260 Therefore, although ACIs decrease RHI with increasing AESF, the ice water path (IWP) shows an increasing



trend with the AESF. Apparently, ARIs reduce the CWP and the decrease in CWP becomes significant with increasing AESF (Figures 9a and 9b), which is mainly caused by the decrease of RHW due to ARIs (Figure S5a). The impact of ARIs on IWP is insignificant with the AESF less than 1.0, in the range between -1% and 1%. When the AESF exceeding 1.0, ARIs increase the IWP due to ARI-induced increase of RHI in the atmosphere between  
265 4 and 7 km (Figure S5b).

Figure 10a shows the variation of *p-mean* of cloud droplet effective radius ( $R_{effc}$ ) with the AESF in F\_BASE and F\_AR10.  $R_{effc}$  decreases with increasing AESF in the F\_BASE and F\_AR10, which is well consistent with the variation of CND and CWP of cloud droplets. When the AESF exceeds 2.5, ARIs increase  $R_{effc}$  (Figure 10b), which is caused by the ARI-induced decrease in the CND (Figure 8b). When ARIs are not considered in the  
270 F\_AR10, *p-mean* of ice crystal effective radius ( $R_{effi}$ ) increases with increasing AESF, which is caused by the ACI-induced decrease in CND (Figure 8c) and increase in IWP of ice crystals (Figure 9c). However, the increase in  $R_{effi}$  is not significant, i.e., when the AESF increases from 0.125 to 8.0, the  $R_{effi}$  increases by about 2.0% (Figure 10c). In addition, the impact of ARIs on the  $R_{effi}$  is insignificant, and the variation in the  $R_{effi}$  is less than 0.2% (Figure 10d).

### 275 3.5 Aerosol effects on precipitation in GZB and GZBs

Considering the difference in aerosol concentrations between GZB and GZBs, we discuss the impact of aerosols on precipitation in each region separately. Figure 11a provides the variation of the average 3-day accumulative precipitation in the GZB with the AESF. When ARIs are not considered in the F\_AR10, the precipitation shows an increasing trend with the AESF, which is not consistent with the results of previous studies  
280 (e.g., Yang et al., 2013a, b; Bei et al., 2015). Yang et al. (2013a, b) have correlated the decreasing trend of precipitation inside the GZB with deterioration of the air pollution, revealing the microphysically suppressive effect of increased aerosols on precipitation. Bei et al. (2025) have also shown that ACIs tend to decrease convective precipitation in the GZB based on sensitivity simulations of a summertime short-term heavy rainfall event. In this study, as we have discussed above, increasing anthropogenic emissions decrease CWP and  $R_{effc}$ ,  
285 lowering the conversion of cloud water to rainwater to decrease the liquid-phase precipitation. However, increasing emissions increase IWP and  $R_{effi}$ , facilitating the formation and growth of snow flakes to enhance the ice-phase precipitation. Figure 12 shows dependence of the liquid-phase and ice-phase precipitation at the ground surface in the GZB with the AESF. Liquid-phase precipitation shows a decreasing trend but ice-phase precipitation shows an increasing trend with the AESF. However, the increase of ice-phase precipitation exceeds  
290 the decrease of liquid-phase precipitation, causing the increasing trend of the accumulative precipitation with the AESF in the GZB (Figure 11a).

ARIs decrease the precipitation with the AESF less than 0.6 and increases it when the AESF is more than 0.6 in the GZB (Figure 11b). ARIs considerably decrease liquid-phase precipitation and the decrease is more than 50% with the AESF greater than 1.0 (Figure 12b). Except the decreasing CWP and  $R_{effc}$  with increasing the AESF,  
295 the decrease in RHW below 3 km caused by ARIs also contributes to the decreasing trend of liquid-phase precipitation in the GZB (Figure S6a). However, ARIs generally increases the ice-phase precipitation monotonically with increasing AESF (Figure 12c). ARI-induced increase in IWP can partially explain the increase in ice-phase precipitation with the AESF exceeding 0.6. Another possible reason is that ARI-induced increase in RHI facilitates survival ice-phase particles when they fall off from clouds (Figure S6b). The decrease in liquid-



300 phase precipitation exceeds the increase in ice-phase precipitation when the AESF is less than 0.6 and it is opposite with the AESF more than 0.6 (Figures 12b and 12d).

In the GZBs, without ARIs, ACIs decrease precipitation with increasing AESF (Figure 11c), and ARIs also appreciably decrease the precipitation with the same AESF (Figures 11c and 11d), which are generally contrary to those in the GZB (Figures 11a and 11b). There are two reasons that can explain the different responses of  
305 precipitation to ARIs and ACIs in the GZB and GZBs. In the F\_ARI0 without ARIs, the variation of liquid-phase and ice-phase precipitation with increasing AESF in the GZBs is similar to those in the GZB. However, the ratio of liquid-phase precipitation to the total precipitation varies considerably in the GZB and GZBs. For example, in the REF0, the ratio in the GZB is 2.5%, but in the GZBs, it is 9.1%. Meanwhile, when ARIs are excluded, ACIs decrease the liquid-phase precipitation by 50% when the AESF increases from 0.125 to 8.0 in the GZBs (Figure  
310 13). Although ACIs increase the ice-phase precipitation with increasing the AESF, the increase is less than the decrease in liquid-phase precipitation, causing the decreasing trend of precipitation with the AESF in the GZBs. In addition, ARIs decrease the liquid-phase and ice-phase precipitation in the GZBs with the same AESF (Figures 13b and 13d), This reduction is attributed to the ARI-induced decrease of RHW and RHI in the atmosphere below 3km (Figure S7), which would enhance the evaporation of precipitation particles.

315 Figure 14 presents the 3-day accumulative precipitation distribution under different AESF (0.125, 1.0, and 8.0) in the F\_ARI0 and F\_BASE. Generally, increasing anthropogenic aerosols do not change the whole precipitation pattern significantly, i.e., the decrease in precipitation from north to south and the occurrence of heavy precipitation in the southeast of GZB+GZBs. However, the variation of different precipitation levels can be observed, for example, the increase in the area with precipitation between 5.0 and 10.0 mm in the GZB and the  
320 decrease in the area with precipitation exceeding 10.0 mm in the south. We also classify the simulated daily precipitations into slight (more than 0.0 and less than 0.1 mm d<sup>-1</sup>), light (0.1-2.5 mm d<sup>-1</sup>), moderate (2.5-5.0 mm d<sup>-1</sup>), and heavy (more than 5.0 mm d<sup>-1</sup>) snowfall according to the Chinese national standard GB/T 28592-2012 Grade of precipitation. In GZB+GZBs, increasing aerosols increase occurrence of slight and light precipitation but decrease moderate and heavy precipitation (Figure S8).

#### 325 4 Summary and conclusions

Using a cloud-resolving fully coupled WRF-Chem model, this study investigated a heavy snowfall event occurred in GZB+GZBs from 26 to 28 January 2022, with a focus on disentangling the roles of ACIs and ARIs under different aerosol loadings. The model reasonably reproduces the observed temporal variation and spatial distribution of air pollutants, as well as the hourly precipitation rate and three-day accumulated precipitation in  
330 the study region.

Sensitivity results reveal that ARIs generally cool the lower atmosphere but cause a warming effect in the middle and upper atmosphere in GZB+GZBs. This vertical thermal adjustment is accompanied by secondary downward motion within the PBL and upward motion aloft, leading to corresponding vertical redistribution of water vapor.

335 When ARIs are excluded, increasing anthropogenic emissions raise CND of cloud droplets, but decrease LWP which is caused by ACI-induced decrease of RHW. While ACI-induced decrease in RHI reduces CND of ice crystals with increasing emissions, and the increasing trend of IWP with the AESF is mainly caused by enhanced collection of cloud water by ice crystals.



340 The response of precipitation to ARIs and ACIs is different in GZB and GZBs. In the GZB, excluding ARIs  
leads to a weak increase in three-day accumulated precipitation with increasing emissions. Although increasing  
aerosols considerably decrease the liquid-phase precipitation, the ACI-induced increase in ice-phase precipitation  
outweighs the decrease in liquid-phase precipitation. ARIs increase the precipitation in the GZB when the AESF  
exceeds 0.6, due to ARI-induced increase in RHI which increase IWP and facilitate survival ice-phase particles  
in the atmosphere. In contrast, precipitation in the GZBs decreases with increasing aerosols, reflecting the  
345 dominance of liquid-phase precipitation that is strongly suppressed by ACIs and further reinforced by ARI-  
induced reductions in RHI. Increasing anthropogenic emissions do not substantially alter the precipitation pattern  
in GZB+GZBs, but can modify the frequency distribution of precipitation intensity.

**Code and data availability.** The hourly ambient surface O<sub>3</sub>, NO<sub>2</sub> and PM<sub>2.5</sub> mass concentrations are real-time  
350 released by Ministry of Environmental Protection, China on the website <http://www.aqistudy.cn/>, freely  
downloaded from <http://106.37.208.233:20035/> (China MEP, 2013). Precipitation observations at meteorological  
sites with rain gauge in the GZBs are from China Meteorological Administration, which can be accessed at  
<https://data.cma.cn/data/cdcdetail/dataCode/A.0012.0001.html>.

355 **Author contributions.** GL and NB, as the corresponding author, provided the ideas and financial support, verified  
the conclusions, and revised the paper. YY conducted research, designed the experiments, performed the  
simulation, processed the data, prepared the data visualization, and prepared the manuscript, with contributions  
from all authors. RW and QJ provided the data and primary data processing and reviewed the manuscript. HH  
validated the model performance, analyzed the study data, and reviewed the manuscript. ZL analyzed the initial  
360 simulation data. XT reviewed the manuscript and provided critical comments.

**Competing interests.** The authors declare that they have no conflict of interest.

**Financial support.** This work is financially supported by the National Key Research and Development Program  
365 of China (grant no. 2022YFF0802502), the National Natural Science Foundation of China (grant no. 41975175),  
and the Key Research and Development Program of Shaanxi (grant no. 2024SF-ZDCYL-05-05).



## References

- Ackerman, A. S., Toon, O. B., Stevens, D. E., Heymsfield, A. J., Ramanathan, V., and Welton, E. J.: Reduction  
370 of tropical cloudiness by soot, *Science*, 288, 1042–1047, <https://doi.org/10.1126/science.288.5468.1042>,  
2000.
- Ackerman, A. S., Toon, O. B., Stevens, D. E., and Coakley Jr., J. A.: Enhancement of cloud cover and suppression  
of nocturnal drizzle in stratocumulus polluted by haze, *Geophys. Res. Lett.*, 30, 1381,  
<https://doi.org/10.1029/2002GL016634>, 2003.
- 375 Albrecht, B. A.: Aerosols, cloud microphysics, and fractional cloudiness, *Science*, 245, 1227–1230,  
<https://doi.org/10.1126/science.245.4923.1227>, 1989.
- An, Z., Huang, R. J., Zhang, R., Tie, X., Li, G., Cao, J., Zhou, W., Shi, Z., Han, Y., and Gu, Z.: Severe haze in  
northern China: A synergy of anthropogenic emissions and atmospheric processes, *P. Natl. Acad. Sci. USA*,  
116, 8657–8666, <https://doi.org/10.1073/pnas.1900125116>, 2019.
- 380 Bai, Y., Li, J., Guo, J., Xu, H., and Wang, Y.: Simulation of the responses of rainstorm in the Yangtze River  
Middle Reaches to changes in anthropogenic aerosol emissions, *Atmos. Environ.*, 220, 117081,  
<https://doi.org/10.1016/j.atmosenv.2019.117081>, 2020.
- Bei, N., Li, G., Huang, R., Cao, J., Meng, N., Feng, T., Liu, S., Zhang, T., Zhang, Q., and Molina, L. T.: Typical  
synoptic situations and their impacts on the wintertime air pollution in the Guanzhong Basin, China, *Atmos.*  
385 *Chem. Phys.*, 16, 7373–7387, <https://doi.org/10.5194/acp-16-7373-2016>, 2016a.
- Bei, N., Xiao, B., Meng, N., and Feng, T.: Critical role of meteorological conditions in a persistent haze episode  
in the Guanzhong Basin, China, *Sci. Total Environ.*, 550, 273–284,  
<https://doi.org/10.1016/j.scitotenv.2016.01.124>, 2016b.
- Bei, N., Wu, J., Elser, M., Feng, T., Cao, J., El-Haddad, I., Li, X., Huang, R. J., Li, Z., Long, X., Zhao, S., Tie,  
390 X., Prévôt, A. S. H., and Li, G.: Impacts of meteorological uncertainties on the haze formation in Beijing–  
Tianjin–Hebei (BTH) during wintertime: a case study, *Atmos. Chem. Phys.*, 17, 14579–14591,  
<https://doi.org/10.5194/acp-17-14579-2017>, 2017.
- Bei, N., Xiao, B., Wang, R., Yang, Y., Liu, L., Han, Y., and Li, G.: Impacts of aerosol–radiation and aerosol–  
cloud interactions on a short-term heavy-rainfall event – a case study in the Guanzhong Basin, China, *Atmos.*  
395 *Chem. Phys.*, 25, 10931–10948, <https://doi.org/10.5194/acp-25-10931-2025>, 2025.
- Boucher, O., Randall, D., Artaxo, P., Bretherton, C., Feingold, G., Forster, P., Kerminen, V., Kondo, Y., Liao, H.,  
and Lohmann, U.: Clouds and aerosols, in *Climate change 2013: The physical science basis. Contribution of  
working group I to the fifth assessment report of the intergovernmental panel on climate change*, Cambridge  
University Press, 571–657, <https://doi.org/10.1017/CBO9781107415324.016>, 2013.
- 400 Braham, R. R., Jr.: Cloud physics of urban weather modification—a preliminary report, *Bull. Amer. Meteor. Soc.*,  
55, 100–106, 1974.
- Cao, Q., Jiang, B., Shen, X., et al.: Microphysics effects of anthropogenic aerosols on urban heavy precipitation  
over the Pearl River Delta, China, *Atmos. Res.*, 253, 105478,  
<https://doi.org/10.1016/j.atmosres.2021.105478>, 2021.
- 405 Chen, T., Li, Z., Kahn, R. A., Zhao, C., Rosenfeld, D., Guo, J., Han, W., and Chen, D.: Potential impact of aerosols  
on convective clouds revealed by Himawari-8 observations over different terrain types in eastern China,  
*Atmos. Chem. Phys.*, 21, 6199–6220, <https://doi.org/10.5194/acp-21-6199-2021>, 2021.



- Feng, T., Bei, N., Zhao, S., Bei, N. F., et al.: Wintertime nitrate formation during haze days in the Guanzhong Basin, China: a case study, *Environ. Pollut.*, 243, 1057–1067, <https://doi.org/10.1016/j.envpol.2018.09.070>,  
410 2018.
- Garrett, T. J., and Zhao, C.: Increased Arctic cloud longwave emissivity associated with pollution from mid-latitudes, *Nature*, 440, 787–789, <https://doi.org/10.1038/nature04636>, 2006.
- Guo, L., Fu, D., Xiao, H., Zhang, Y., and Miao, S.: Numerical analysis of the impact of complex urban environment on a snowfall event in Beijing, *J. Geophys. Res.-Atmos.*, 126, e2021JD035442,  
415 <https://doi.org/10.1029/2021JD035442>, 2021.
- Guo, J., Deng, M., Fan, J., Li, Z., Chen, Q., Zhai, P., Dai, Z., and Li, X.: Precipitation and air pollution at mountain and plain stations in northern China: insights gained from observations and modeling, *J. Geophys. Res.-Atmos.*, 119, 4793–4807, <https://doi.org/10.1002/2013JD021161>, 2014.
- Guo, J., Liu, H., Li, Z., Rosenfeld, D., Jiang, M., Xu, W., Jiang, J. H., He, J., Chen, D., Min, M., and Zhai, P.:  
420 Aerosol-induced changes in the vertical structure of precipitation: a perspective of TRMM precipitation radar, *Atmos. Chem. Phys.*, 18, 13329–13343, <https://doi.org/10.5194/acp-18-13329-2018>, 2018.
- Huang, X., and Ding, A.: Aerosol as a critical factor causing forecast biases of air temperature in global numerical weather prediction models, *Sci. Bull.*, 66, 1917–1924, <https://doi.org/10.1016/j.scib.2021.05.009>, 2021.
- Huo, F., Liu, Y., Li, R., Wang, Y., Li, Z., Zhang, Y., and He, Q.: Reduction in autumn precipitation over Southwest  
425 China by anthropogenic aerosol emissions from eastern China, *Atmos. Res.*, 257, 105627, <https://doi.org/10.1016/j.atmosres.2021.105627>, 2021.
- IPCC: Climate Change 2013: The Physical Science Basis. Contribution of Working Group I to the Fifth Assessment Report of the Intergovernmental Panel on Climate Change, Cambridge University Press, Cambridge, UK and New York, NY, USA, <https://doi.org/10.1017/CBO9781107415324>, 2013.
- 430 IPCC: Climate Change 2021: The Physical Science Basis. Contribution of Working Group I to the Sixth Assessment Report of the Intergovernmental Panel on Climate Change, Cambridge University Press, Cambridge, UK and New York, NY, USA, <https://doi.org/10.1017/9781009157896>, 2021.
- Khain, A., Rosenfeld, D., and Pokrovsky, A.: Aerosol impact on the dynamics and microphysics of deep convective clouds, *Q. J. Roy. Meteorol. Soc.*, 131, 2639–2663, <https://doi.org/10.1256/qj.04.62>, 2005.
- 435 Khain, A., BenMoshe, N., and Pokrovsky, A.: Factors determining the impact of aerosols on surface precipitation from clouds: an attempt at classification, *J. Atmos. Sci.*, 65, 1721–1748, <https://doi.org/10.1175/2007JAS2515.1>, 2008.
- Koren, I., Kaufman, Y. J., Remer, L. A., and Martins, J. V.: Measurement of the effect of Amazon smoke on inhibition of cloud formation, *Science*, 303, 1342–1345, <https://doi.org/10.1126/science.1089424>, 2004.
- 440 Li, G., Lei, W., Zavala, M., Volkamer, R., Dusanter, S., Stevens, P., and Molina, L. T.: Impacts of HONO sources on the photochemistry in Mexico City during the MCMA-2006/MILAGO Campaign, *Atmos. Chem. Phys.*, 10, 6551–6567, doi:10.5194/acp-10-6551-2010, 2010.
- Li, G., Bei, N., Tie, X., and Molina, L. T.: Aerosol effects on the photochemistry in Mexico City during MCMA-2006/MILAGRO campaign, *Atmos. Chem. Phys.*, 11, 5169–5182, doi:10.5194/acp-11-5169-2011, 2011a.
- 445 Li, G., Zavala, M., Lei, W., Tsimpidi, A. P., Karydis, V. A., Pandis, S. N., Canagaratna, M. R., and Molina, L. T.: Simulations of organic aerosol concentrations in Mexico City using the WRF-CHEM model during the



- MCMA-2006/MILAGRO campaign, *Atmos. Chem. Phys.*, 11, 3789–3809, doi:10.5194/acp-11-3789-2011, 2011b.
- Li, G., Lei, W., Bei, N., and Molina, L. T.: Contribution of garbage burning to chloride and PM<sub>2.5</sub> in Mexico City, *Atmos. Chem. Phys.*, 12, 8751–8761, doi:10.5194/acp-12-8751-2012, 2012.
- Menon, S., Hansen, J., Nazarenko, L., and Luo, Y.: Climate effects of black carbon aerosols in China and India, *Science*, 297, 2250–2253, <https://doi.org/10.1126/science.1075159>, 2002.
- Mitchell Jr., J. M.: The effect of atmospheric aerosols on climate with special reference to temperature near the earth's surface, *J. Appl. Meteorol. Climatol.*, 10, 703–714, [https://doi.org/10.1175/1520-0450\(1971\)010<0703:TEOAAO>2.0.CO;2](https://doi.org/10.1175/1520-0450(1971)010<0703:TEOAAO>2.0.CO;2), 1971.
- Moch, J. M., Mickley, L. J., Keller, C. A., Bian, H., Lundgren, E. W., Zhai, S., and Jacob, D. J.: Aerosol-radiation interactions in China in winter: Competing effects of reduced shortwave radiation and cloud-snowfall-albedo feedbacks under rapidly changing emissions, *J. Geophys. Res.-Atmos.*, 127, e2021JD035442, <https://doi.org/10.1029/2021JD035442>, 2022.
- Moraglia, G., and Crippa, P.: Assessing the influence of aerosols on urban precipitation: a sensitivity study of Dallas–Fort Worth, *Atmos. Res.*, 328, 108436, <https://doi.org/10.1016/j.atmosres.2024.108436>, 2026.
- Öktem, R., Romps, D. M., and Varble, A. C.: No warm-phase invigoration of convection detected during GoAmazon, *J. Atmos. Sci.*, 80, 2345–2364, <https://doi.org/10.1175/JAS-D-22-0241.1>, 2023.
- Peng, H., Hu, X., Ai, W., Qiao, J., and Zhao, X.: Effects of fine and coarse aerosols on the summer precipitation structure and microphysics over the Yangtze River Delta region, *Atmos. Res.*, 326, 108277, doi:10.1016/j.atmosres.2025.108277, 2025.
- Pinsky, M., Mazin, I. P., Korolev, A., and Khain, A.: Supersaturation and diffusional droplet growth in liquid clouds, *J. Atmos. Sci.*, 70, 2778–2793, <https://doi.org/10.1175/JAS-D-12-077.1>, 2013.
- Pravia-Sarabia, E., Montávez, J. P., Halifa-Marin, A., Jiménez-Guerrero, P., and Gómez-Navarro, J. J.: The Role of Aerosol Concentration on Precipitation in a Winter Extreme Mixed-Phase System: The Case of Storm Filomena, *Remote Sens.*, 15, 1398, doi:10.3390/rs15051398, 2023.
- Twomey, S.: The influence of pollution on the shortwave albedo of clouds, *J. Atmos. Sci.*, 34, 1149–1152, [https://doi.org/10.1175/1520-0469\(1977\)034<1149:TIOPOP>2.0.CO;2](https://doi.org/10.1175/1520-0469(1977)034<1149:TIOPOP>2.0.CO;2), 1977.
- Romps, D. M., Latimer, K., Zhu, Q., Jurkat-Witschas, T., Mahnke, C., Prabhakaran, T., et al.: Air pollution unable to intensify storms via warm-phase invigoration, *Geophys. Res. Lett.*, 50, e2022GL100409, <https://doi.org/10.1029/2022GL100409>, 2023.
- Rosenfeld, D.: TRMM observed first direct evidence of smoke from forest fires inhibiting rainfall, *Geophys. Res. Lett.*, 26, 3105–3108, <https://doi.org/10.1029/1999GL010556>, 1999.
- Rosenfeld, D., Lohmann, U., Raga, G. B., O'Dowd, C. D., Kulmala, M., Fuzzi, S., Reissell, A., and Andreae, M. O.: Flood or drought: how do aerosols affect precipitation?, *Science*, 321, 1309–1313, <https://doi.org/10.1126/science.1160606>, 2008.
- Ryu, Y.-H., and Min, S.-K.: Greenhouse warming and anthropogenic aerosols synergistically reduce springtime rainfall in low-latitude East Asia, *NPJ Clim. Atmos. Sci.*, 5, 69, <https://doi.org/10.1038/s41612-022-00278-9>, 2022.

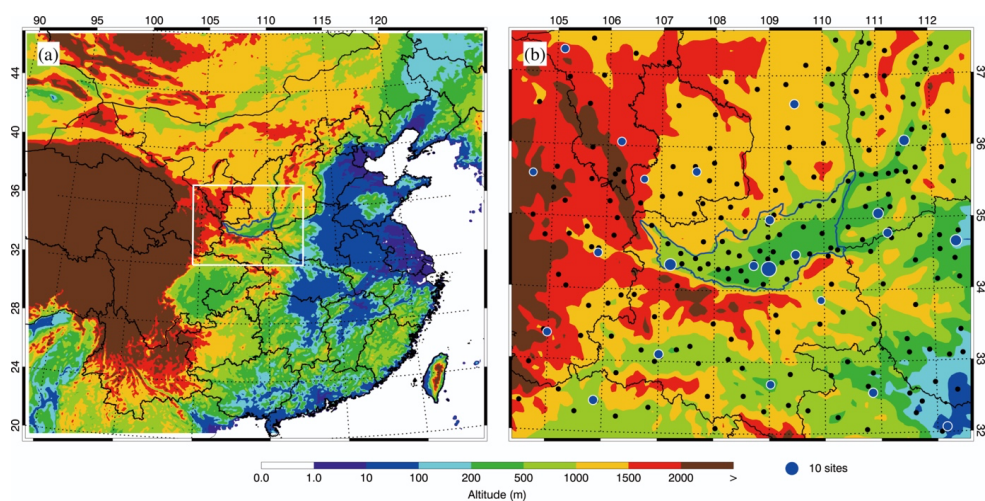


- 485 Saleeby, S. M., Cotton, W. R., and Fuller, J. D.: The cumulative impact of cloud droplet nucleating aerosols on orographic snowfall in Colorado, *J. Appl. Meteorol. Climatol.*, 50, 599–612, <https://doi.org/10.1175/2010JAMC2498.1>, 2010.
- Shao, T., Zhang, H., Xu, X., Li, J., Wu, S., and Liu, Y.: Role of anthropogenic aerosols in affecting different-grade precipitation over eastern China: a case study, *Sci. Total Environ.*, 807, 150886, <https://doi.org/10.1016/j.scitotenv.2021.150886>, 2022.
- 490 Shen, Z., Cao, J., Liu, S., Zhu, C., Wang, X., Zhang, T., Xu, H., and Hu, T.: Chemical composition of PM10 and PM2.5 collected at ground level and 100-m during a strong winter-time pollution episode in Xi'an, China, *J. Air Waste Manage.*, 61, 1150–1159, <https://doi.org/10.1080/10473289.2011.607490>, 2011.
- Sun, N., Wu, H., Luo, Y., Zhao, C., and Li, Z.: Aerosol effects on the vertical structure of precipitation in East  
495 China, *NPJ Clim. Atmos. Sci.*, 5, 60, <https://doi.org/10.1038/s41612-022-00271-2>, 2022.
- Sun, Y., and Zhao, C.: Distinct impacts on precipitation by aerosol radiative effect over three different megacity regions of eastern China, *Atmos. Chem. Phys.*, 21, 16555–16574, <https://doi.org/10.5194/acp-21-16555-2021>, 2021.
- Tao, W. K., Li, X. W., Khain, A., Matsui, T., and Lang, S.: Role of atmospheric aerosol concentration on deep  
500 convective precipitation: cloud-resolving model simulation, *J. Geophys. Res.-Atmos.*, 112, D24S18, <https://doi.org/10.1029/2007JD008728>, 2007.
- Thompson, G., and Eidhammer, T.: A study of aerosol impacts on clouds and precipitation development in a large winter cyclone, *J. Atmos. Sci.*, 71, 3636–3658, <https://doi.org/10.1175/JAS-D-13-0305.1>, 2014.
- Varble, A. C., Igel, A. L., Morrison, H., Grabowski, W. W., and Lebo, Z. J.: Opinion: A critical evaluation of the  
505 evidence for aerosol invigoration of deep convection, *Atmos. Chem. Phys.*, 23, 13791–13808, <https://doi.org/10.5194/acp-23-13791-2023>, 2023.
- Wang, W., Chen, G., and Zhang, Y.: Role of aerosol ice-nucleus effect in the development of the “21·7” Henan extreme precipitation, *J. Geophys. Res.-Atmos.*, 129, e2024JD041487, <https://doi.org/10.1029/2024JD041487>, 2024.
- 510 Wang, Y., Wan, Q., Meng, W., Liao, F., Tan, H., and Wang, D.: Impacts of aerosols on weather and regional climate over the Pearl River Delta megacity area in China, *Atmos. Chem. Phys.*, 11, 5837–5852, <https://doi.org/10.5194/acp-11-5837-2011>, 2011.
- Xiao, Z., Zhu, S., Miao, Y., et al.: On the relationship between convective precipitation and aerosol pollution in North China Plain during autumn and winter, *Atmos. Res.*, 271, 106120, <https://doi.org/10.1016/j.atmosres.2021.106120>, 2022.
- 515 Xie, X., Tang, S., Liu, X., Wang, Y., and Wang, Y.: Anthropogenic sulfate aerosol pollution in South and East Asia induces increased summer precipitation over arid Central Asia, *Commun. Earth Environ.*, 3, 328, <https://doi.org/10.1038/s43247-022-00605-7>, 2022.
- Yang, X., Ferrat, M., and Li, Z.: New evidence of orographic precipitation suppression by aerosols in central  
520 China, *Meteorol. Atmos. Phys.*, 119, 17–29, <https://doi.org/10.1007/s00703-012-0221-9>, 2013a.
- Yang, X., Yao, Z., Li, Z., and Fan, T.: Heavy air pollution suppresses summer thunderstorms in central China, *J. Atmos. Sol. Terr. Phys.*, 95, 28–40, <https://doi.org/10.1016/j.jastp.2012.12.023>, 2013b.
- Yang, X., and Li, Z.: Increases in thunderstorm activity and relationships with air pollution in southeast China, *J. Geophys. Res.-Atmos.*, 119, 1835–1844, <https://doi.org/10.1002/2013JD021224>, 2014.

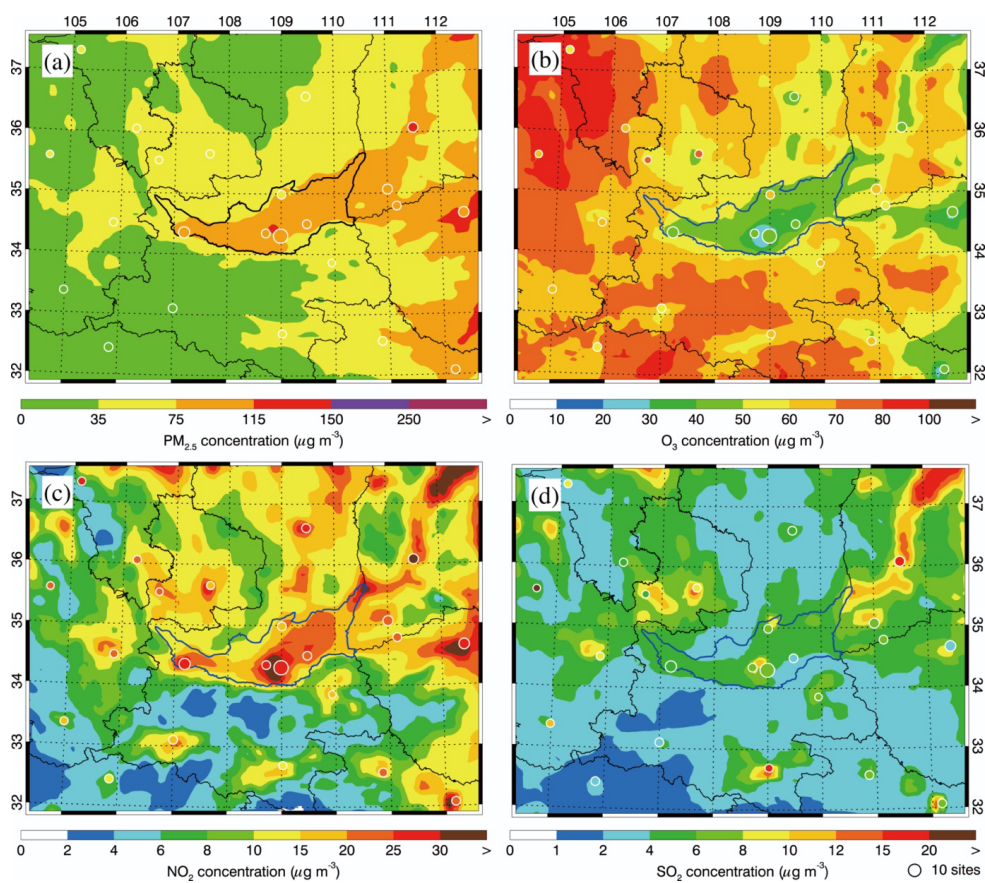


- 525 Yun, Y., Zhang, D.-L., Gao, W., et al.: Spatiotemporal variations of the effects of aerosols on clouds and precipitation in an extreme-rain-producing MCS in South China, *J. Geophys. Res.-Atmos.*, 129, e2023JD040014, <https://doi.org/10.1029/2023JD040014>, 2024.
- Zhang, L., Wu, P., and Zhou, T.: Aerosol forcing of extreme summer drought over North China, *Environ. Res. Lett.*, 12, 034020, <https://doi.org/10.1088/1748-9326/aa5fb0>, 2017.
- 530 Zhang, W., Wang, H., Zhang, X., et al.: Aerosol–cloud interaction in the atmospheric chemistry model GRAPES\_Meso5.1/CUACE and its impacts on mesoscale numerical weather prediction under haze pollution conditions in Jing–Jin–Ji in China, *Atmos. Chem. Phys.*, 22, 15207–15221, <https://doi.org/10.5194/acp-22-15207-2022>, 2022.
- Zhang, Y., Easter, R. C., Ghan, S. J., and Abdul-Razzak, H.: Impact of aerosol size representation on modeling aerosol–cloud interactions, *J. Geophys. Res.-Atmos.*, 107, 4558, <https://doi.org/10.1029/2001JD001549>, 2002.
- 535 Zhao, C., Yang, Y., Fan, H., Huang, J., Fu, Y., Zhang, X., Kang, S., Cong, Z., Letu, H., and Menenti, M.: Aerosol characteristics and impacts on weather and climate over Tibetan Plateau, *Natl. Sci. Rev.*, 7, 492–495, <https://doi.org/10.1093/nsr/nwz184>, 2020.
- 540 Zhao, C., Sun, Y., Yang, J., Li, J., Zhou, Y., Yang, Y., Fan, H., and Zhao, X.: Observational evidence and mechanisms of aerosol effects on precipitation, *Sci. Bull.*, 69, 1569–1580, <https://doi.org/10.1016/j.scib.2024.03.014>, 2024.
- Zhou, Y., Zhao, C., and Sun, Y.: A modeling study of aerosol effect on summer nocturnal convective precipitation in Beijing, *Atmos. Res.*, 305, 107430, <https://doi.org/10.1016/j.atmosres.2024.107430>, 2024.

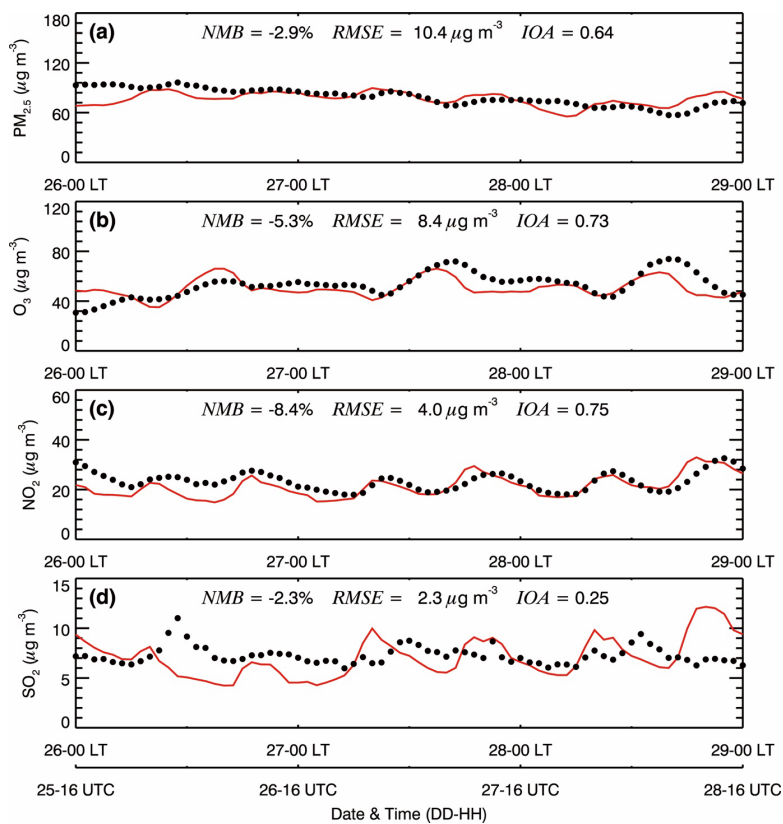
545



550 **Figure 1: (a) WRF-Chem simulation domain with topography and (b) Guanzhong basin (GZB, the area surrounded by blue lines) and its surrounding areas (GZBs, the area excluding GZB). In (b), the black dots denote the meteorological sites with rain gauge and the blue dots denote centers of cities with air pollutants observations and the size of blue circles denotes the number of ambient monitoring sites of cities.**



555 **Figure 2: Pattern comparisons of simulated (color counters) vs. observed (colored dots) average near-surface mass concentrations of (a) PM<sub>2.5</sub>, (b) O<sub>3</sub>, (c) NO<sub>2</sub> and (d) SO<sub>2</sub> from 26 to 28 January 2022.**



560

Figure 3: Comparison of observed (black dots) and simulated (solid red lines) diurnal profile of near-surface hourly mass concentrations of (a)  $\text{PM}_{2.5}$ , (b)  $\text{O}_3$ , (c)  $\text{NO}_2$ , and (d)  $\text{SO}_2$  averaged at monitoring sites in GZB+GZBs from 26 to 28 January 2022.

565

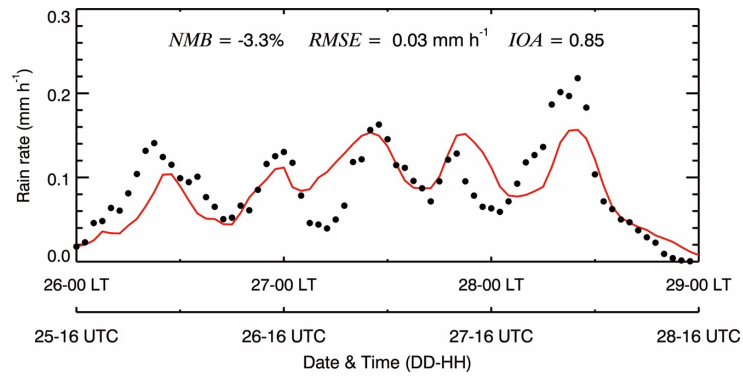
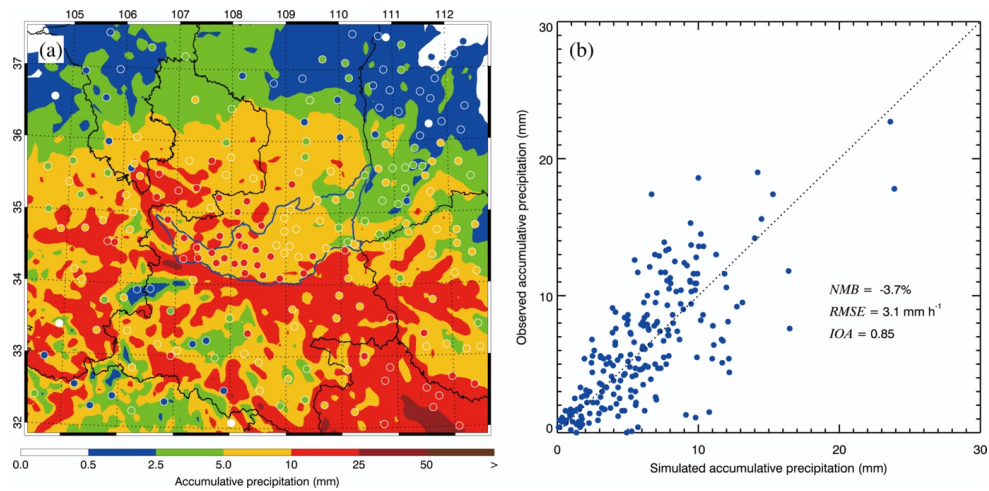
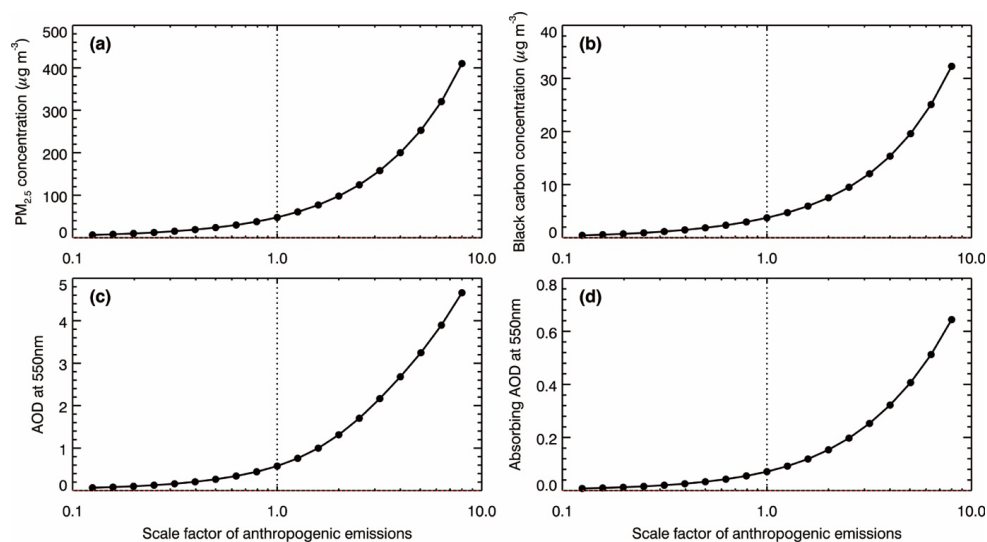


**Figure 4: Comparison of observed (black dots) and simulated (solid red lines) diurnal profile of hourly rain rate averaged at monitoring sites in GZB+GZBs from 26 to 28 January 2022.**

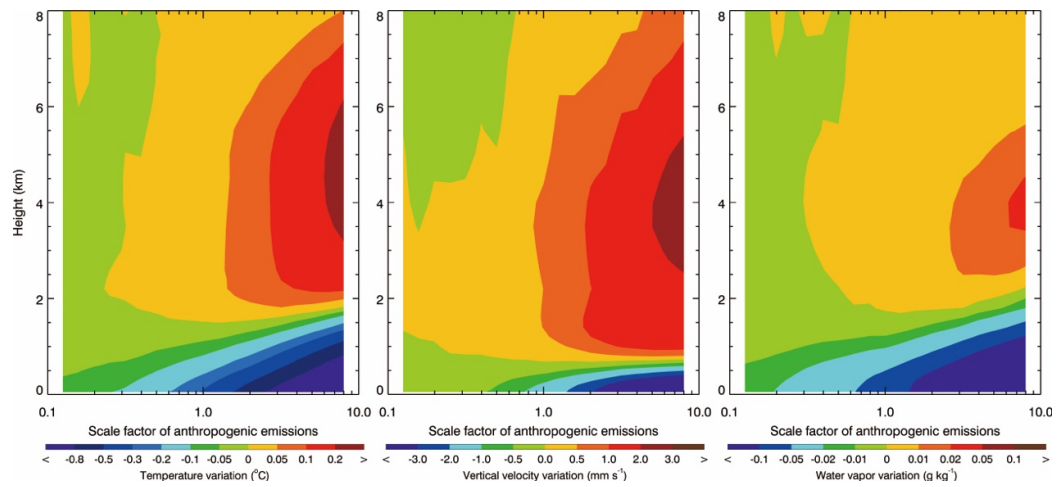
570



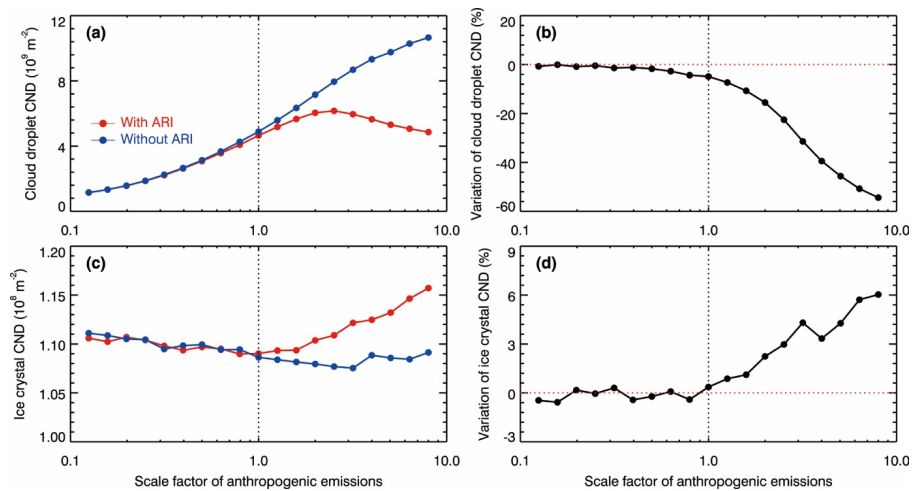
575 **Figure 5: (a) Pattern comparisons of simulated (color counters) vs. observed (colored dots) accumulative precipitation, and (b) scatter plot of simulated and observed accumulative precipitation in GZB+GZBs from 26 to 28 January 2022.**



580 Figure 6: Average (a) near-surface  $PM_{2.5}$  (b) black carbon mass concentration, (c) AOD at 550nm, and (d) absorbing AOD at 550 nm in GZB+GZBs from 26 to 28 January 2022, as a function of the scale factor of anthropogenic emissions.



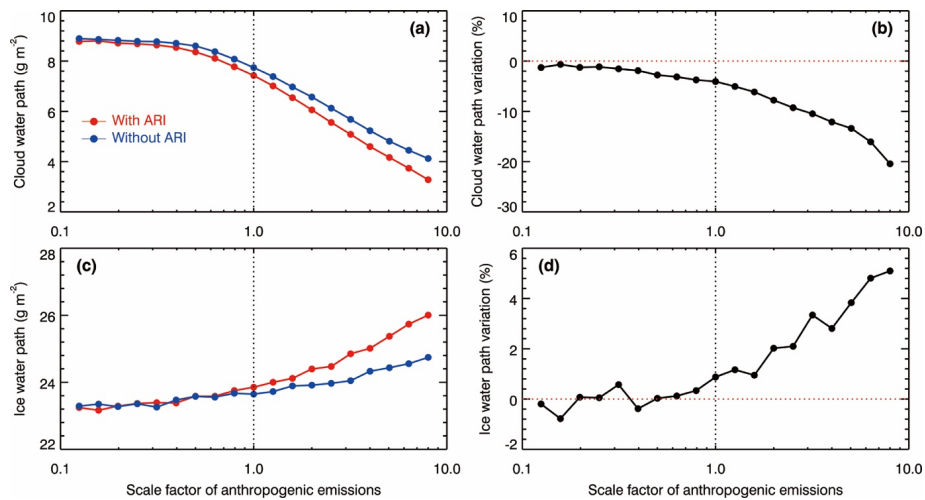
585 **Figure 7: Profile variation of average (a) air temperature, (b) vertical velocity, and (c) water vapor over GZB+GZBs from 26 to 28 January 2022 caused by ARIs, as a function of the scale factor of anthropogenic emissions.**



590

**Figure 8: Average (a) cloud droplet CND, (b) variation of cloud droplet CND due to ARIs, (c) ice crystal CND, and (d) variation of ice crystal CND due to ARIs over GZB+GZBs from 26 to 28 January 2022, as a function of the scale factor of anthropogenic emissions.**

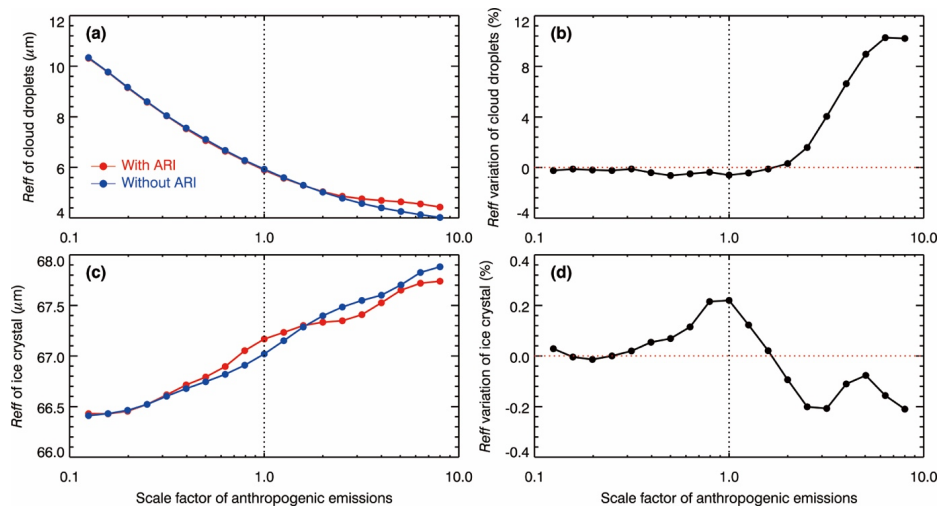
595



600

**Figure 9: Average (a) CWP, (b) variation of CWP due to ARIs, (c) IWP, and (d) variation of IWP due to ARIs over GZB+GZBs from 26 to 28 January 2022, as a function of the scale factor of anthropogenic emissions.**

605



610 **Figure 10: (a)  $p$ -mean of  $R_{eff,c}$ , (b) variation of  $p$ -mean of  $R_{eff,c}$  due to ARIs, (c)  $p$ -mean of  $R_{eff,i}$ , and (d) variation of  $p$ -mean of  $R_{eff,i}$  due to ARIs over GZB+GZBs from 26 to 28 January 2022, as a function of the scale factor of anthropogenic emissions.**

615

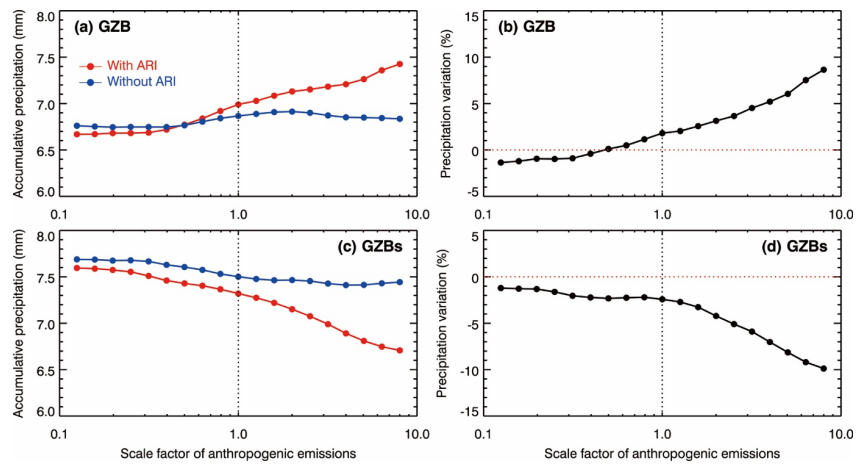
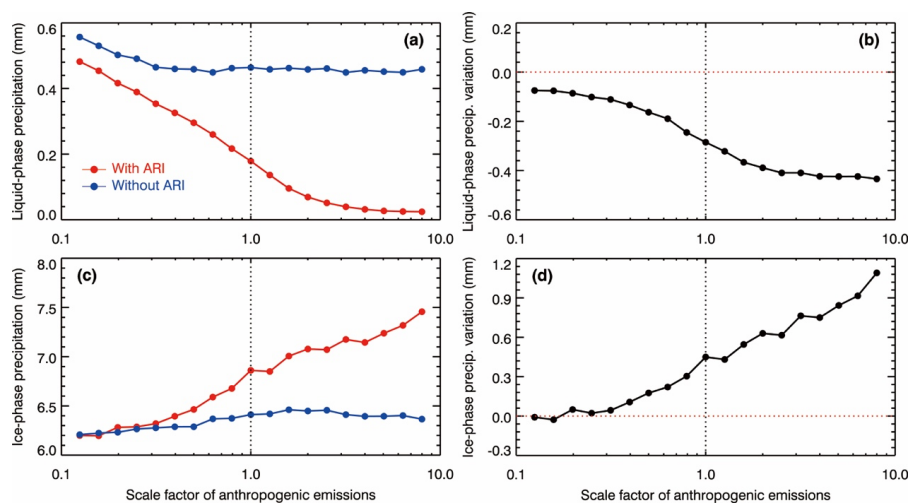
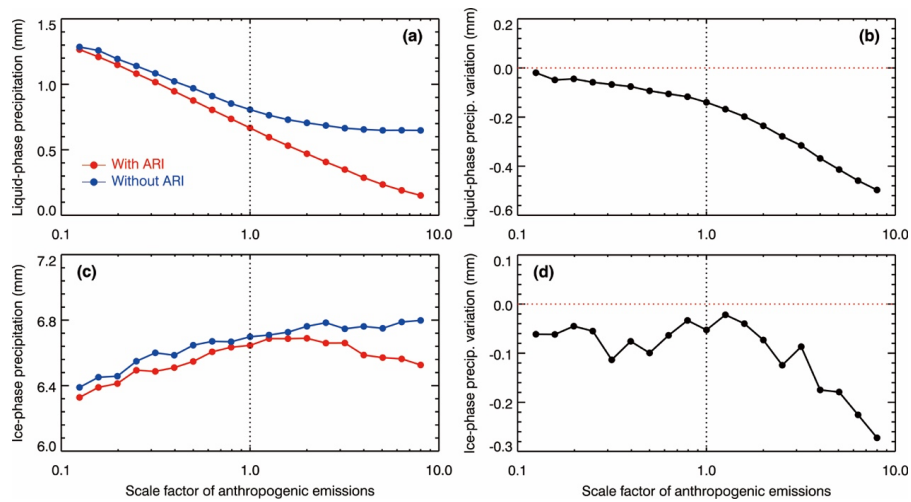


**Figure 11: Average accumulative precipitation in (a) GZB and (c) GZBs, and variation of precipitation due to ARIs in (b) GZB and (d) GZBs from 26 to 28 January 2022, as a function of the scale factor of anthropogenic emissions.**

620

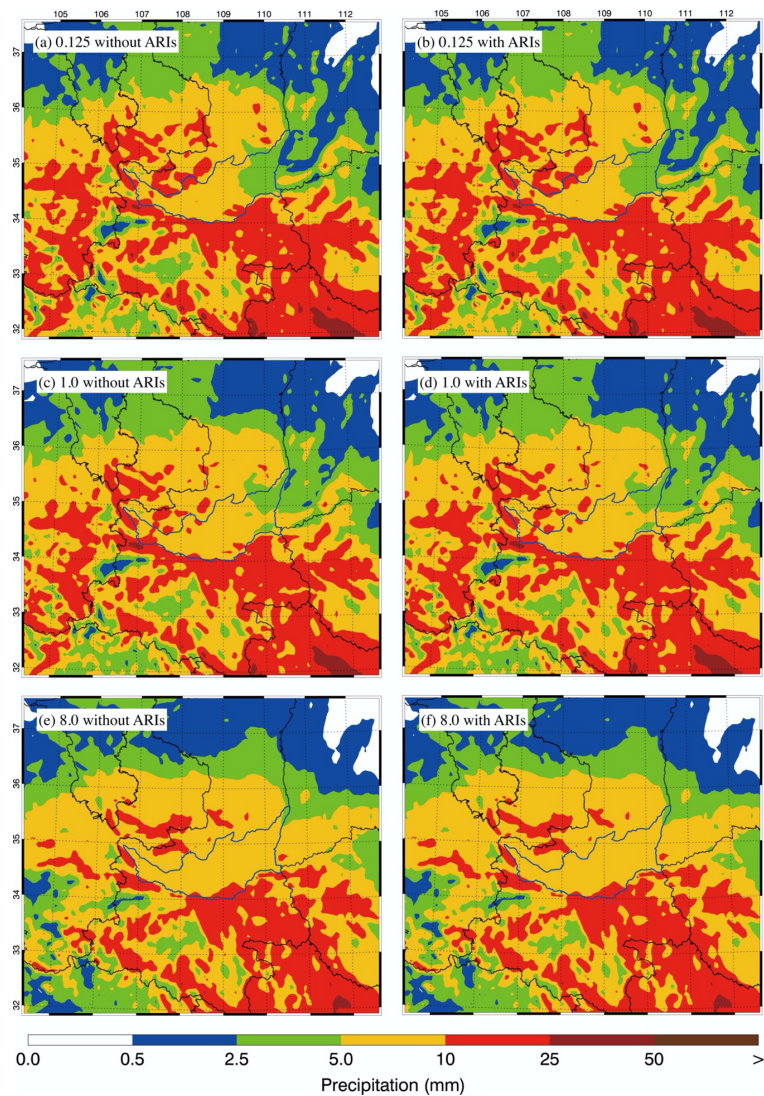


625 **Figure 12: Average accumulative (a) liquid-phase and (c) ice-phase precipitation, and variation of (b) liquid-phase and (d) ice-phase precipitation due to ARIs in GZB from 26 to 28 January 2022, as a function of the scale factor of anthropogenic emissions.**



630 **Figure 13: Average accumulative (a) liquid-phase and (c) ice-phase precipitation, and variation of (b) liquid-phase and (d) ice-phase precipitation due to ARIs in GZBs from 26 to 28 January 2022, as a function of the scale factor of anthropogenic emissions.**

635



640 **Figure 14: Distribution of accumulative precipitation from 26 to 28 January 2022 for various scale factor of anthropogenic emissions when ARIs are (a), (c), and (e) excluded and (b), (d), and (f) included.**